10184 *Biochemistry* **2006,** *45,* 10184−10190

Articles

Structural Characterization of Enterobactin Hydrolase IroE[†,‡]

N. A. Larsen,[§] H. Lin,[§,⊥] R. Wei,[§] M. A. Fischbach,[§,||] and C. T. Walsh*[,§]

Department of Biological Chemistry and Molecular Pharmacology, Harvard Medical School, 240 Longwood Avenue,
Boston, Massachusetts 02115-5702, and Department of Chemistry and Chemical Biology, Howard Hughes Medical Institute,
12 Oxford Street, Cambridge, Massachusetts 02138

Received May 12, 2006; Revised Manuscript Received June 24, 2006

ABSTRACT: The proliferation of many pathogenic bacteria is limited by the scarcity of soluble iron in their environment. Many of these bacteria scavenge iron by synthesizing and exporting small molecule siderophores that chelate iron. Iron-bound siderophores are subsequently imported for metabolic processing. Three related serine hydrolases have been characterized biochemically in this pathway: Fes, IroD, and IroE. Here, we report the crystal structure of IroE from uropathogenic *Escherichia coli* CFT073. The native structure and a complex with diisopropyl fluorophosphonate (DFP, a potent serine hydrolase inhibitor) were determined at 2.3 and 1.4 Å resolution, respectively. IroE has the typical α/β-hydrolase fold with an atypical catalytic dyad composed of Ser 189 and His 287. Mutation of either residue was detrimental to catalysis. In addition, rather than the typical oxyanion hole composed of backbone amides, IroE employs the atypical guanidinium moiety of Arg 130. Asp 90 anchors Arg 130 in the active site, and mutation of either residue was likewise detrimental to catalysis. We also compare the structure of IroE to the structure of Fes from *Shigella flexneri* (PDB entry 2B20). Both enzymes have similar active sites, but Fes has an additional amino-terminal lid domain. These lid domains are proposed to confer specificity to these related hydrolases.

Most bacteria require iron as a cofactor in biocatalysis, yet the concentration of ferric ions in water is limited to 10^{-18} M. In mammalian cells, the concentration of ferric ions is further reduced to an estimated 10^{-24} M by endogenous iron-binding proteins (*1*). To obtain iron, many pathogenic bacteria have evolved metabolic pathways to synthesize, transport, and process small molecules, termed siderophores, that can chelate iron with high affinities (*2*). The archetypal chelator is enterobactin (Ent),[1] a cyclic trilactone composed of three dihydroxybenzoylserine (DHB) monomers (Figure 1).

Ent is assembled in the cytoplasm by a nonribosomal peptide synthetase and subsequently transported into the periplasm by the membrane protein EntS and into the environment by TolC (Figure 2A). The uptake of iron-bound (holo) Ent into the periplasm requires FepA, and final transport to the cytoplasm is mediated by membrane proteins FepD and -G and driven by FepC-mediated ATP hydrolysis (reviewed in ref *3*). In the cytoplasm, the esterase Fes exhaustively hydrolyzes the trilactone scaffold to release the ferric ion into the cytoplasm (Figure 2A) (*4*).

Despite the high affinity of Ent for iron, the efficiency of holo-Ent uptake is compromised in vivo, because mammalian hosts have at least one innate defense mechanism. Serum protein lipocalin 2 (also called neutrophil gelatinase-associated lipocalin or 24p3) binds holo-Ent with high affinity, preventing uptake by the bacteria (*5*). Recently, C-glucosylated Ent derivatives, termed salmochelins, were identified from *Salmonella* strains (Figure 1) (*6*, *7*). The C-glucosylation of Ent is mediated by C-glucosyl transferase IroB (Figure 2B), one of five proteins encoded by the *iroA* gene cluster (*8*). This form of molecular camouflage helps Ent evade the innate defenses of the host (*3*). Apo salmochelins are predicted to be exported to the periplasm by IroC, and holo salmochelins are imported by receptor IroN (*3*). The holo samochelins are no longer substrates for Fes but rather are substrates for the related esterase IroD (Figure 2B) (*4*). IroD likewise prefers holo over apo salmochelins as substrates (*4*). Thus, enterobactin and salmochelin siderophores are processed in related parallel pathways (Figure 2A,B).

Interestingly, in the *iroA* cluster, a second esterase, IroE, exists. IroE is predicted to be a periplasmic membrane

---

[†] This research was supported by postdoctoral fellowships from the Jane Coffin Childs Memorial Fund for medical research (N.A.L. and H.L.), a predoctoral fellowship from the Hertz Foundation (M.A.F.), and NIH Grant AI042738 (C.T.W.).

[‡] The atomic coordinates and structure factors for IroE have been deposited for immediate release in the Protein Data Bank as entries 2GZR (native) and 2GZS (DFP complex).

[*] To whom correspondence should be addressed. E-mail: christopher_walsh@hms.harvard.edu. Phone: (617) 432-1715. Fax: (617) 432-0438.

[§] Harvard Medical School.

[||] Howard Hughes Medical Institute.

[⊥] Current address: Department of Chemistry and Chemical Biology, Cornell University, Ithaca, NY 19853.

[1] Abbreviations: DFP, diisopropyl fluorophosphonate; Ent, enterobactin; DHB, dihydroxybenzoylserine; IPTG, isopropyl 1-thio-β-D-galactopyranoside.

10.1021/bi060950i CCC: $33.50

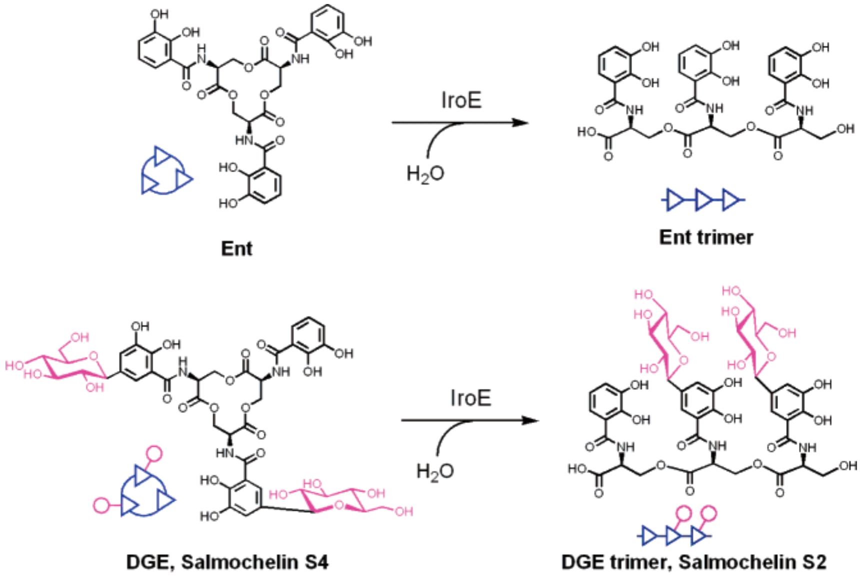

FIGURE 1: Structures of Ent, DGE, and their IroE hydrolysis products. The symbols consisting of blue triangles and pink circles are used to represent these compounds. IroE-catalyzed hydrolysis of DGE produces at least two regio-isomers of the DGE linear trimer. Here only one of them is shown.

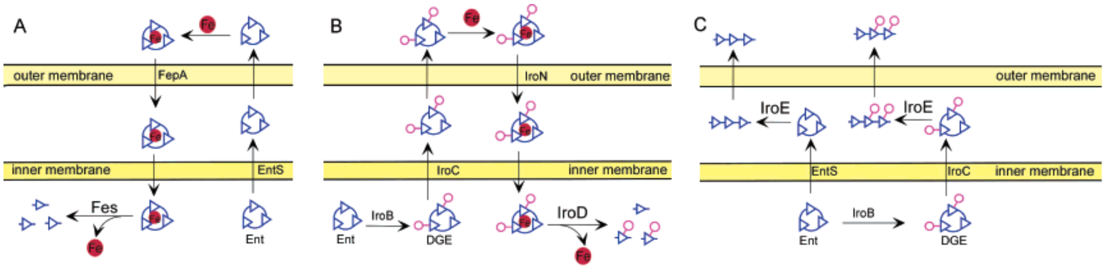

FIGURE 2: Biochemical functions of Fes, IroD, and IroE. (A) In the Ent pathway, holo-Ent is degraded by Fes in the cytoplasm to release iron. (B) In the salmochelin pathway, Ent is glycosylated by IroB and exported. Holo-DGE is degraded by IroD located in the cytoplasm. (C) IroE is likely a periplasmic protein and catalyzes the hydrolysis of apo siderophores to produce linearized trimers, which are then secreted. The holo-S4 trimer is imported back to the cytoplasm and degraded by IroD to release iron.

protein, with residues 13−32 anchored in the bilayer. We have proposed that the physiological substrate for IroE is the apo siderophore, which is cleaved a single time to form the linear trimer (Figures 1 and 2C) (*4*). This hypothesis is supported by several observations. First, IroE hydrolyzes the apo form with at least 16-fold enhanced catalytic efficiency ($k_{cat}K_M^{-1}$) over the holo form, and the hydrolysis of holo siderophores is inhibited by substrate at high substrate concentrations, in vitro (*4*). Second, the linear siderophores are more abundant in the culture media than the cyclic form, while the cyclic form predominates in *iroE* deletion strains (*6*, *7*). These linearized siderophores still chelate iron with an only slightly reduced affinity. On the basis of these in vitro and in vivo observations, a model in which IroE linearizes siderophores for export (Figure 2C), perhaps to provide a more diverse array of chelators with which to challenge the host (*3*), has been proposed.

Despite the differing siderophore specificity of IroE, IroD, and Fes, these esterases share sequence similarity. Structure determination was initiated to gain insights into the mode of catalysis and the origin of their differing specificity and to provide a framework for further exploring the molecular logic of this pathway. Here, we report the crystal structure of IroE from uropathogenic *Escherichia coli* CFT073, including the native structure and a covalent complex with diisopropyl fluorophosphonate (DFP). We also compare the structure of IroE to that of Fes from *Shigella flexneri* (PDB entry 2B20).

MATERIALS AND METHODS

Expression and Purification. IroE from uropathogenic *E. coli* CFT073 was amplified from a genomic library and subcloned via primer-derived NdeI and EcoRI restriction sites into pET-28b(+) (Novagen), in frame with the vector-encoded N-terminal His$_6$ tag and thrombin cleavage site. The cloned construct began with residue 41 to facilitate crystallization and because residues 13−32 were predicted to anchor IroE to the periplasmic membrane. IroE mutants were constructed using a two-step PCR procedure (staggered overlap extension). The identities of the IroE mutants were confirmed by DNA sequencing. The constructs were transformed into *E. coli* BL21(DE3) cells, and protein expression and purification were as described previously (*4*).

Se-Met-substituted IroE was overexpressed in BL834(DE3) methionine auxotroph cells (Novagen) by induction with 1 mM isopropyl 1-thio-β-D-galactopyranoside (IPTG) at an OD of ~0.8 for 4 h at 23 °C. Soluble IroE was purified from bacterial lysate by Ni−NTA chromatography (Qiagen). The His tag was removed by overnight digestion with thrombin (1 unit/mg of IroE) at 4 °C. The digest reaction mixture was further purified by size exclusion chromatography on an S200 16/60-Sephadex column (Pharmacia)

Table 1: Data and Refinement Statistics

	apo	DFP λ1 (f″)	DFP λ2 (f′)	DFP λ3
wavelength	0.9796	0.9796	0.9798	0.9184
resolution (Å)	2.3	1.4	1.4	1.4
no. of unique observations	19495	79460	79454	80486
redundancy[a]	1.8 (1.5)	1.9 (1.6)	1.9 (1.6)	1.9 (1.9)
completeness[a]	93.6 (80.8)	94.0 (86.3)	94.1 (86.3)	95.3 (94.2)
I/σ[a]	12.0 (2.6)	17.8 (2.9)	18.0 (2.8)	17.6 (3.5)
R_{sym}[b]	6.0 (19.5)	3.6 (19.4)	5.1 (20.4)	3.6 (16.7)

	apo	DFP
refinement statistics		
no. of refined residues	239	246
no. of refined waters	71	197
R_{cryst}[c]	20.3	17.4
R_{free}[d]	26.8	18.6
average B values (Å^2)		
IroE	30.7	18.8
DFP	NA	20.3
waters	32.9	37.9
Ramachandran statistics (%)		
most favored	87.3	92.9
additional allowed	11.7	5.7
generously allowed	0.0	0.5
disallowed	1.0[e]	0.9[e]

[a] Numbers in parentheses refer to the highest-resolution shell. [b] $R_{sym} = [\sum_h \sum_i |I_i(h) - \langle I(h)\rangle| / \sum_h \sum_i I_i(h)] \times 100$, where $\langle I(h)\rangle$ is the average intensity of i symmetry-related observations of reflections with Bragg index h. [c] $R_{cryst} = (\sum_{hkl}|F_o - F_c| / \sum_{hkl}|F_o|) \times 100$, where F_o and F_c are the observed and calculated structure factors, respectively. [d] R_{free} was calculated as for R_{cryst}, but on 5% of the data excluded before refinement. [e] The nucleophile Ser 189 is in a strained conformation, consistent with other hydrolases.

equilibrated in 10 mM NaCl, 10 mM HEPES (pH 7.5), and 10 mM β-Me. The peak fractions were pooled and concentrated to 16 mg/mL in the presence of 10 mM DTT to retard the facile air oxidation of selenium.

Enzymatic Activity Assay of Mutants. All enzymatic activity assays were carried out in 100 μL of 75 mM HEPES buffer (pH 7.5) with 64 μM Ent or DGE. Enzyme concentrations ranged from 100 nM (for the wild type and mutants with activity similar to that of the wild type) to several micromolar (for mutants with very low activity). Hydrolysis reactions were allowed to proceed for either 1 min (for the wild type and mutants with activity similar to that of the wild type) or 10 min (for mutants with very low activity). The reactions were quenched by the addition of 100 μL of 1.5 N HCl in a 2:1 methanol/water mixture, and then the mixtures were analyzed by reverse phase HPLC, monitoring at 316 nm.

Crystallization, Structure Determination, and Refinement. IroE was concentrated to 16 mg/mL in 10 mM NaCl, 10 mM HEPES (pH 7.5), and 10 mM DTT. Initial IroE crystals were obtained using the HydraII crystallization robot (Matrix Technologies). In this format, sitting drops containing 0.5 μL of protein and 0.5 μL of precipitant are equilibrated by vapor diffusion over a 90 μL reservoir of precipitant. These initial crystals were further optimized by hand. In this format, hanging drops containing 5 μL of protein and 5 μL of precipitant are equilibrated by vapor diffusion over a 1 mL reservoir of precipitant. Crystals grew as thin plates in 6−10% PEG 3350 and 100 mM HEPES (pH 7.5). An IroE protein solution incubated with 500 mM DFP formed chunkier crystals under the same conditions. Native and DFP derivative crystals were frozen after immersion in a 20% (v/v) ethylene glycol-substituted cryoprotectant. MAD data were collected to 1.4 Å resolution on Advanced Light Source (ALS) beamline 8.2.1 (Table 1). The data were processed in HKL2000 (*9*) as $P1$ with the following unit cell dimensions: $a = 36.6$ Å, $b = 38.8$ Å, $c = 44.4$ Å, $\alpha = 113.2°$, $\beta = 93.6°$, and $\gamma = 98.7°$. A calculated solvent content of 32% with one molecule per unit cell was found.

IroE contains four selenomethionines, all of which were sufficiently ordered to obtain phases and an interpretable electron density map for the entire molecule in space group $P1$. Initial sites were obtained from the MAD data using SOLVE (*10*). The phases were extended to high resolution, and 80% of the molecule was built using Arp/Warp (*11*), with an additional 10% traced by hand in O (*12*). Coordinates for DFP were obtained from PDB entry 1CI9 (*13*) and modeled into the electron density. The native structure was refined with CNS (*14*), while the DFP derivative structure was refined with SHELX (*15*) (Table 1).

RESULTS

IroE Is an α/β-Hydrolase. The crystallized construct of IroE from uropathogenic *E. coli* CFT073 contains 278 amino acids with a molecular mass of ∼30800 Da. IroE is a monomer in solution and is also a monomer in the crystal lattice. The DFP−IroE adduct was obtained by cocrystallization with 500 mM DFP. The DFP complex was phased by multiwavelength anomalous diffraction (MAD) methods from a Se-Met derivative (Table 1) to 2.1 Å and phase extended to 1.4 Å resolution. The native enzyme was determined by molecular replacement at 2.3 Å resolution using the DFP complex as a search model. The final models contain three regions of disorder, localized to loop regions and the last 13 C-terminal residues.

IroE has a single domain with the canonical α/β-hydrolase fold. The fold consists of repeating β−α−β motifs that form a central, predominantly parallel (except β2), eight-stranded β-sheet (strand order β1, β2, β4, β3, β5, β6, β7, β8)

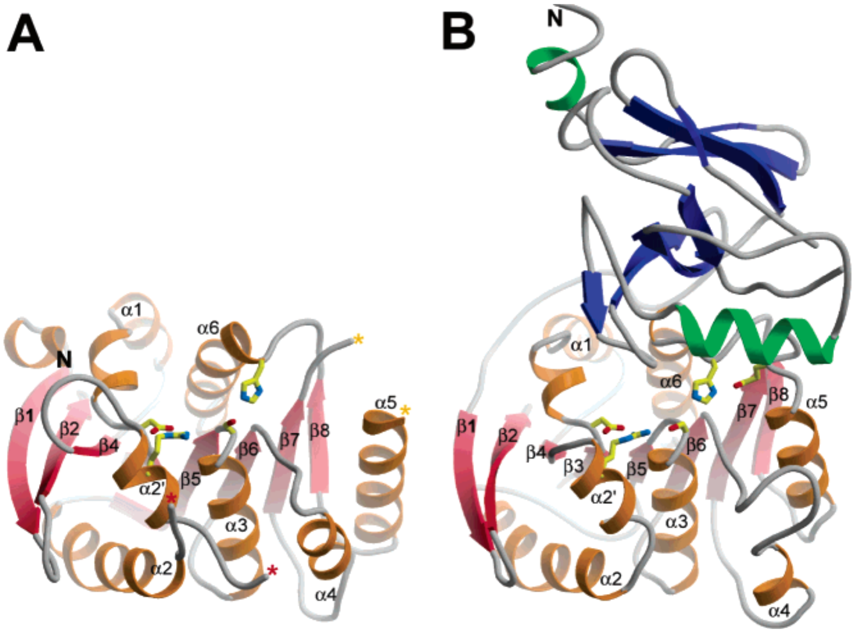

FIGURE 3: Crystal structures of IroE and Fes. (A) Ribbon diagram of IroE. IroE has a single α/β-hydrolase domain (orange and red). The amino terminus is labeled N. Breaks in the electron density are illustrated with asterisks. Strand β3 and the C-terminus are occluded in this view. Active site residues are rendered as sticks. (B) Ribbon diagram of Fes (PDB entry 2B20). The molecule is shown in the same orientation as IroE using superposition matrices derived from DALI. The α/β-hydrolase domain and active site residues are colored and rendered similarly. Fes has an amino-terminal β-sandwich lid domain over the active site (green and blue). This figure was generated in Bobscript (*32*) and rendered with Raster3d (*33*).

surrounded on either side by α-helices (Figure 3A). The core β-sheet has a right-handed twist, and the β−α−β motifs are likewise right-handed, except for the unusual left-handed junction between strand β8 and helix α6. This unusual topology is a hallmark of the α/β-hydrolase fold and is necessary to properly position the catalytic histidine residue in the active site (*16*). In the hydrolase family of enzymes, insertions are commonly observed in the canonical structure at the amino and carboxyl termini and at the junction between strands β6 and β7. Such insertions are believed to be the determinants for the substrate specificity of the enzyme (*16*, *17*). IroE has relatively short insertions, a simple helix−turn−strand motif at the amino terminus that extends the central β-sheet by an extra strand (β1′), and a 20-amino acid loop insertion between strands β4 and β5 (Figure 3A). This latter insertion forms a mobile “lid” over the back of the active site, not all of which could be resolved in the electron density.

IroE Is Homologous to Fes. Enterochelin esterase Fes from *S. flexneri* (PDB entry 2B20) had the highest level of structural homology to IroE (Figure 3B), as determined by the highest DALI *Z* score of 20 (*18*). According to this algorithm, a *Z* score of >12 has significant homology. The structural alignment for the two enzymes gives a rmsd of 2.8 Å over 206 equivalent Cα atoms (residues 47−303 in IroE and 153−392 in Fes) and a 18% level of sequence identity in the same range. The major topological difference between the two enzymes is in the large (150 amino acids) amino-terminal lid domain in Fes, which is predominantly a globular β-structure with two α-helices (Figure 3B). This large domain covers part of the active site and presumably is important for substrate recognition. This large lid domain gives Fes a much deeper binding pocket. In contrast, the binding pocket for IroE is relatively shallow and exposed.

IroE Has an Atypical Catalytic Dyad. Crystals grown in 500 mM DFP (diisopropyl fluorophosphonate) yielded a tetrahedral covalent adduct between Oγ of Ser 189 and phosphate (Figure 4A,B). Comparison with this adduct and the native structure led to immediate identification of two of the prototypic catalytic triad residues, Ser 189 and His 287, at the carboxyl end of strands β5 and β8, respectively. Ser 189 is located in the conserved GX$_1$SX$_2$G motif (GHSYG), a signature sequence for the hydrolase family (*16*). The Ser 189 Ala and His 287 Ala mutants were both inactive (Table 2). No carboxylate was observed in the electron density interacting with His 287. In nearly all members of the hydrolase fold, an Asp or Glu located at the end of strand β7 interacts with the catalytic His at the end of strand β8. In IroE, the corresponding region between β7 and helix αE was disordered. The Fes structure has similar active site residues, and the region between β7 and αE is ordered and contains a catalytic Glu 345 interacting with His 375.

Sequence alignments of related IroE enzymes show that there is no Asp or Glu that is completely conserved between β7 and αE. Indeed, the only two possibilities for a carboxylate in this region are Asp 250 or Glu 253. The Asp 250 Asn, Asp 250 Ala, and Glu 253 Ala mutants all retained activity, excluding them as candidates for being a catalytic residue (Table 2). Superposition of the Fes structure on IroE shows that Glu 345 of Fes superimposes on Ser 245 of IroE. Considering that IroE has a lower catalytic efficiency (k_{cat}/K_m) than Fes, we wondered whether the Ser 245 Asp/Glu mutants would have higher activities than wild-type IroE. However, a biochemical assay indicates that both mutants have slightly lower activities than the wild type. These data also suggest that Ser 245 is unlikely to be critical for catalysis. Thus, our data support the idea that IroE lacks a fully functional catalytic triad and rather contains an atypical catalytic dyad.

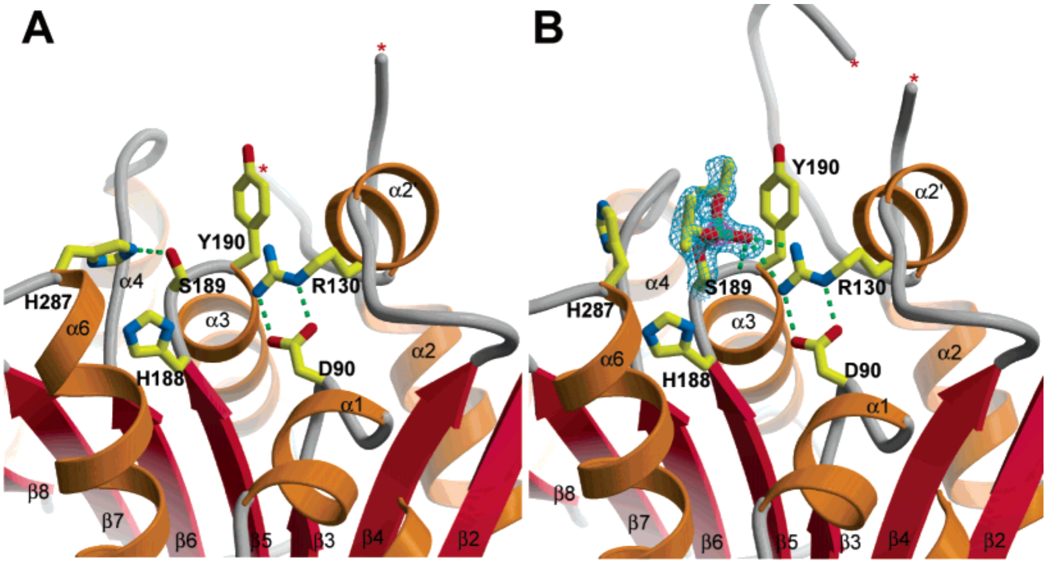

FIGURE 4: Comparison of native and complex structures. (A) Active site residues of IroE. H-Bonds are represented as dashed green lines. In the native structure, Ser 189 forms a H-bond to His 287. Asp 90 anchors Arg 130 in the oxyanion hole. (B) DFP forms an adduct with Ser 189. The isopropyl group pushes the side chain of His 287 away from Ser 189. The $2F_o - F_c$ electron density map around the DFP molecule is contoured at 1.2σ (blue) and 5σ (magenta).

Table 2: Relative Activity of Mutants

	relative activity on Ent hydrolysis	relative activity on DGE hydrolysis
wild type[a]	1.0	1.0
S189A	0.00005	0.00014
H287A	0.0001	0.00037
D250N	0.72	0.62
D250A	0.59	0.72
E253Q	0.92	0.97
E253A	0.78	0.86
S245E	0.84	0.66
S245D	0.60	0.60
D90N	0.015	0.015
D90A	0.004	0.0056
R130K	0.0036	0.0041
R130Q	0.00015	0.00024

[a] The activity (v $[\text{IroE}]^{-1}$) of wild-type Ent is 204 min^{-1} and for DGE is 170 min^{-1}.

IroE Has an Unusual Arginine Oxyanion Hole. In the DFP−IroE adduct, the divalent phosphonate oxygen is in a tridentate oxyanion hole, where it forms hydrogen bonds with the backbone amides of Tyr 190, and the NH1 and NH2 atoms from the guanidinium moiety of Arg 130 located in αB1, the helix that caps the active site just after strand β4. The active site serine of IroE is located in the so-called nucleophilic elbow, where the backbone ϕ and ψ angles ($-\phi$ and $-\psi$) have evolved strain to place the adjoining backbone amide in the oxyanion hole. IroE also employs the Arg side chain in the oxyanion hole. The guanidinium moiety of Arg 130 is anchored exquisitely in the active site by a salt bridge interaction with Asp 90 (Figure 3). Mutation of Arg to either Lys or Gln leads to an inactive enzyme (Table 2). On the basis of simple modeling, the Nz atom of Lys would superimpose on the Cz atom of Arg, resulting in a predicted 0.8 Å displacement of the oxyanion hole. Here, the oxyanion hole is positioned carefully so that this relatively small displacement of the bond from the NH group of Arg to the Nz atom of Lys is sufficient to annul the catalytic activity. In addition, mutation of Asp 90 to either Asn or Ala abrogates activity. On the basis of these data, we propose that Asp 90 is essential for anchoring Arg 130 to form the oxyanion hole. Superposition with Fes shows the same Arg 240−Asp 201 pair, which is expected to play a similar role in catalysis (Figure 3).

Overall, the native and complex structures closely superimpose (rmsd = 1.1 Å for all Cα atoms). There is a modest conformational rearrangement in the loop region between strand β6 and helix α4, as well as a modest shift in the loop between strand β8 and helix α6. The latter movement is probably minimally functionally significant as it is a direct result of steric interaction between the bulky isopropyl group of DFP and the imidazole side chain of the catalytic His 287.

DISCUSSION

The crystal structure of IroE shows that the enzyme has a canonical α/β-hydrolase fold with an atypical catalytic dyad, a shallow binding pocket, and an atypical oxyanion hole. The generally accepted role for the carboxylate is to stabilize the imidazolium ion that develops on the catalytic His in the transition state of the reaction. In principle, this stabilization of the imidazolium ion should increase the pK_a of the catalytic His. In a classic study of the active site His of subtilisin, it was shown that mutation of a nearby carboxylate (Asp 99 Ser) depressed the pK_a of the catalytic His by 0.4 unit (*19*). Therefore, we would expect the pK_a of His 287 in IroE to be lower than that of the corresponding His in IroD and Fes.

In our structure, no other H-bonds to His 287 were seen in the IroE structure except to the nucleophile, Ser 189. In other serine hydrolases, mutating the Asp to either Asn or Ala is detrimental to activity (*20*). Catalytic dyads have been seen in other enzymes, like the *Streptomyces scabies* esterase; however, this enzyme does not have the α/β-hydrolase topology, and the catalytic His forms a H-bond with a backbone carbonyl (*21*). Catalytic dyads have also been seen in some enzymes with carboxypeptidase activities that share the tertiary fold of the β-lactamases (*22*). For these enzymes, the catalytic dyad is composed of Lys and Ser. Type I leader signal peptidases also have a Ser-Lys catalytic dyad, and the related endoplasmic reticulum signal peptidase has a Ser-His dyad (*23*). Thus, catalytic dyads have been seen in related enzyme systems but not in an α/β-hydrolase enzyme.

A major difference between IroE and Fes is the large amino-terminal domain that covers part of the Fes active site. Sequence alignments show that IroD, another esterase in the *iroA* cluster, likewise has a large amino-terminal domain and functional triad, and it is likely that these two enzymes will closely resemble one another. The active site of IroD accommodates bulkier substrates, namely, the glycosylated Ent species. Therefore, we would expect the binding pocket to be larger but similar to that seen in the Fes structure.

The enzymology for Fes and IroD is similar as both enzymes prefer holo siderophores as substrates and exhaustively cleave the trilactone scaffold to DHB−Ser or Glc−DHB−Ser monomers. In contrast, IroE prefers apo siderophores and hydrolyzes the trilactone scaffold only once to give linear trimers (*4*). This observation led, in part, to a model in which IroE linearizes apo siderophores in the periplasm for export, while IroD and Fes degrade holo siderophores in the cytoplasm to release iron. One possibility for this observed difference in activity is that the large lid domain in Fes and IroD helps to retain the hydrolysis intermediates in the active sites so that the hydrolysis reactions occur more processively, resulting in complete degradation of the trilactone scaffold. In contrast, without the large lid domain, IroE releases the linear trimer, which is then a poor substrate for additional hydrolysis.

IroE has no carboxylate charge relay system to stabilize the transition state, and this may explain why the k_{cat} of IroE is 3-fold lower for apo-Ent and 20-fold lower for apo-DGE compared with the corresponding k_{cat} values of IroD, which, like Fes, has a full catalytic triad (*4*). The reduction in k_{cat} and a priori reduction in catalytic efficiency provide some rationale for the single cleavage event observed for IroE. Moreover, IroE also has a shallow binding pocket, while Fes and IroD both have large amino-terminal lid domains that make their binding pockets much deeper. We speculate that this lid domain, coupled with a more efficient triad, may help trap the substrate and initial hydrolysis products for more processive degradation and the ultimate release of iron.

An additional unexpected observation from this family of enterobactin hydrolases is the Arg in the oxyanion hole. To the best of our knowledge, arginine has never been observed in the oxyanion hole of an α/β-hydrolase, and only once in the catalytic triad of cytomegalovirus peptidase, which has an entirely different tertiary structure (*24*). As for IroE, mutation of this peptidase arginine reduced activity by 4 orders of magnitude (*25*). Arginine is also found in the oxyanion hole of carboxypeptidase A (CPA), a zinc metalloprotease (*26*). The CPA Arg 127 Met mutant reduced the activity between 2 and 5 orders of magnitude, depending on the substrate that was assayed (*27*).

In the α/β-hydrolase family, the oxyanion hole is usually composed of backbone amides (*17*). In the hormone sensitive lipase (HSL) family of hydrolases, for example, three backbone amides contribute to the oxyanion hole (*28*). Scattered reports of Tyr in the oxyanion hole have been documented for prolyl oligopeptidase (*29*) and the cocaine hydrolase CocE from rhodococcal strain MB1 (*30*). For the CocE enzyme, mutation of the Tyr to Phe renders the catalytic activity immeasurably slow (*31*). We observe the same detrimental loss of activity for the Arg to Gln mutation as well as the Arg to Lys mutations in IroE. Stabilization of the oxyanion during the transition state is arguably as important for catalysis as the catalytic triad itself. How the oxyanion hole evolves is probably subject to the constraints imposed by the topology of the enzyme as well as the pK_a demands of the transition state. Presumably, the residues of the oxyanion hole are optimized to make the strongest possible hydrogen bonds that would stabilize the oxyanion in the transition state.

From our structural data, we can begin to rationalize the substrate specificity differences in trilactone hydrolysis patterns of IroE compared to those of Fes and IroD. A complete understanding of the detailed interactions will require additional structures. The key remaining question is the elucidation of the precise biological role of IroE. Comparison of IroE and Fes structures suggests that we can engineer Fes and IroD constructs that lack the amino-terminal lid domain and examine their biochemical properties and their in vivo consequences. Without the lid domain, Fes and IroD would closely resemble IroE, and therefore, such mutants may not be able to complete trilactone processive hydrolysis and release iron from the chelated siderophore. Likewise, we can analyze the in vivo consequence of the inactive IroE mutants and determine the extent to which IroE-mediated linearization of Ent and salmochelin S4 prior to export contributes to the pathogenicity of the *iroA* locus. These crystal structures represent an important step in our understanding of the *iroA* and *fes* biology.

ACKNOWLEDGMENT

We thank Steve Harrison for mentorship and support. We also thank Anastasia Haykov for excellent assistance with protein expression and the Advanced Light Source (ALS) for beam time.

REFERENCES

1. Raymond, K. N., Dertz, E. A., and Kim, S. S. (2003) Enterobactin: An archetype for microbial iron transport, *Proc. Natl. Acad. Sci. U.S.A. 100*, 3584−3588.
2. Crosa, J. H., Mey, A. R., and Payne, S. M. (2004) *Iron Transport in Bacteria*, ASM Press, Washington, DC.
3. Fischbach, M. A., Lin, H., Liu, D. R., and Walsh, C. T. (2006) How pathogenic bacteria evade mammalian sabotage in the battle for iron, *Nat. Chem. Biol. 2*, 132−138.
4. Lin, H., Fischbach, M. A., Liu, D. R., and Walsh, C. T. (2005) In vitro characterization of salmochelin and enterobactin trilactone hydrolases IroD, IroE, and Fes, *J. Am. Chem. Soc. 127*, 11075−11084.
5. Flo, T. H., et al. (2004) Lipocalin 2 mediates an innate immune response to bacterial infection by sequestering iron, *Nature 432*, 917−921.
6. Hantke, K., Nicholson, G. J., Rabsch, W., and Winkelmann, G. (2003) Salmochelins, siderophores of *Salmonella enterica* and uropathogenic *Escherichia coli* strains, are recognized by the outer membrane receptor IroN, *Proc. Natl. Acad. Sci. U.S.A. 100*, 3677−3682.
7. Bister, B., Bischoff, D., Nicholson, G. J., Valdebenito, M., Schneider, K., Winkelmann, G., Hantke, K., and Sussmuth, R. D. (2004) C-Glucosylated enterobactins of *Salmonella enterica*, *Biometals 17*, 471−481.
8. Fischbach, M. A., Lin, H., Liu, D. R., and Walsh, C. T. (2005) In vitro characterization of IroB, a pathogen-associated C-glycosyltransferase, *Proc. Natl. Acad. Sci. U.S.A. 102*, 571−576.

9. Otwinowski, Z., and Minor, W. (1997) Processing of X-ray diffraction data collected in oscilliation mode, *Methods Enzymol. 276*, 307−326.
10. Terwilliger, T. C., and Berendzen, J. (1997) Bayesian MAD phasing, *Acta Crystallogr. D53*, 571−579.
11. Morris, R. J., Perrakis, A., and Lamzin, V. S. (2003) ARP/wARP and automatic interpretation of protein electron density maps, *Methods Enzymol. 374*, 229−244.
12. Jones, T. A., Zou, J. Y., Cowan, S. W., and Kjeldgaard, M. (1991) Improved methods for building protein models in electron density maps and the location of errors in these models, *Acta Crystallogr. A47*, 110−119.
13. Wagner, U. G., Petersen, E. I., Schwab, H., and Kratky, C. (2002) EstB from *Burkholderia gladioli*: A novel esterase with a β-lactamase fold reveals steric factors to discriminate between esterolytic and β-lactam cleaving activity, *Protein Sci. 11*, 467−478.
14. Brünger, A. T., Adams, P. D., Clore, G. M., Delano, W. L., Gros, P., Grosse-Kunstleve, R. W., Jiang, J.-S., Kuszewski, J., Nilges, M., Pannu, N. S., Read, R. J., Rice, L. M., Simonson, T., and Warren, G. L. (1998) Crystallography & NMR System: A new software suite for molecular structure determination, *Acta Crystallogr. D54*, 905−921.
15. Sheldrick, G. M., and Schneider, T. R. (1997) SHELXL: High-resolution refinement, *Methods Enzymol. 277B*, 319−343.
16. Nardini, M., and Dijkstra, B. W. (1999) α/β-Hydrolase fold enzymes: The family keeps growing, *Curr. Opin. Struct. Biol. 9*, 732−737.
17. Heikinheimo, P., Goldman, A., Jeffries, C., and Ollis, D. (1999) Of barn owls and bankers: A lush variety of α/β hydrolases, *Structure 7*, R141−R146.
18. Holm, L., and Sander, C. (1993) Protein structure comparison by alignment of distance matrices, *J. Mol. Biol. 233*, 123−138.
19. Sternberg, M. J., Hayes, F. R., Russell, A. J., Thomas, P. G., and Fersht, A. R. (1987) Prediction of electrostatic effects of engineering of protein charges, *Nature 330*, 86−88.
20. Polgar, L. (2005) The catalytic triad of serine peptidases, *Cell. Mol. Life Sci. 62*, 2161−2172.
21. Wei, Y., Schottel, J. L., Derewenda, U., Swenson, L., Patkar, S., and Derewenda, Z. S. (1995) A novel variant of the catalytic triad in the *Streptomyces scabies* esterase, *Nat. Struct. Biol. 2*, 218−223.
22. Paetzel, M., and Strynadka, N. C. (1999) Common protein architecture and binding sites in proteases utilizing a Ser/Lys dyad mechanism, *Protein Sci. 8*, 2533−2536.
23. Dalbey, R. E., Lively, M. O., Bron, S., and van Dijl, J. M. (1997) The chemistry and enzymology of the type I signal peptidases, *Protein Sci. 6*, 1129−1138.
24. Qiu, X., Culp, J. S., DiLella, A. G., Hellmig, B., Hoog, S. S., Janson, C. A., et al. (1996) Unique fold and active site in cytomegalovirus protease, *Nature 383*, 275−279.
25. Liang, P. H., Brun, K. A., Feild, J. A., O'Donnell, K., Doyle, M. L., Green, S. M., et al. (1998) Site-directed mutagenesis probing the catalytic role of arginines 165 and 166 of human cytomegalovirus protease, *Biochemistry 37*, 5923−5929.
26. Kim, H., and Lipscomb, W. N. (1991) Comparison of the structures of three carboxypeptidase A-phosphonate complexes determined by X-ray crystallography, *Biochemistry 30*, 8171−8180.
27. Phillips, M. A., Fletterick, R., and Rutter, W. J. (1990) Arginine 127 stabilizes the transition state in carboxypeptidase, *J. Biol. Chem. 265*, 20692−20698.
28. Zhu, X., Larsen, N. A., Basran, A., Bruce, N. C., and Wilson, I. A. (2003) Observation of an arsenic adduct in an acetyl esterase crystal structure, *J. Biol. Chem. 278*, 2008−2014.
29. Fulop, V., Bocskei, Z., and Polgar, L. (1998) Prolyl oligopeptidase: An unusual β-propeller domain regulates proteoltsis, *Cell 94*, 161−170.
30. Larsen, N. A., Turner, J. M., Stevens, J., Rosser, S. J., Basran, A., Lerner, R. A., Bruce, N. C., and Wilson, I. A. (2002) Crystal structure of a bacterial cocaine esterase, *Nat. Struct. Biol. 9*, 17−21.
31. Turner, J. M., Larsen, N. A., Basran, A., Barbas, C. F., III, Bruce, N. C., Wilson, I. A., and Lerner, R. A. (2002) Biochemical characterization and structural analysis of a highly proficient cocaine esterase, *Biochemistry 41*, 12297−12307.
32. Esnouf, R. M. (1999) Further additions to MOLSCRIPT version 1.4, including reading and contouring of electron density maps, *Acta Crystallogr. D55*, 938−940.
33. Merritt, E. A., and Murphy, M. E. P. (1994) Raster3D Version 2.0. A program for photorealistic molecular graphics, *Acta Crystallogr. D50*, 869−873.

BI060950I